Article

Microphase Separation Transformation in Bio-Based Benzoxazine/Phenolic/PEO-*b*-PCL Diblock Copolymer Mixtures Induced by Transesterification Reaction

Yang-Chin Kao, Yi-Hsuan Ku, Mohamed Gamal Mohamed, Wei-Hung Su, and Shiao-Wei Kuo*

Cite This: *Macromolecules* 2025, 58, 585–600

Read Online

ACCESS | Metrics & More | Article Recommendations | SI Supporting Information

ABSTRACT: Herein, we synthesized a difunctionalized bio-based vanillin azine monomer (4,4′-((1*E*,1′*E*)-hydrazine-1,2-diylidenebis(methaneylylidene))bis(2-methoxyphenol), VBAZ-2OH) via a Schiff base reaction between vanillin and hydrazine monohydride. Subsequently, we successfully prepared 2,2′-(((1*E*,1′*E*)-hydrazine-1,2-diylidenebis(methaneylylidene))bis(8-methoxy-2*H*-benzo[*e*][1,3]oxazine-6,3(4*H*)-diyl))bis(ethan-1-ol), VBAZ-BZ-2OH), which contains oxazine units, through a Mannich condensation reaction of VBAZ-2OH with ethanolamine and paraformaldehyde in 1,4-dioxane as the solvent. The chemical structures of these two monomers (VBAZ-2OH and VBAZ-BZ-2OH) were characterized by using NMR and FTIR analyses. Our study aimed to investigate the transesterification reactions by blending different VBAZ-BZ-2OH/phenolic resin (BP) compositions with a PEO$_{112}$-*b*-PCL$_{99}$ (EC) diblock copolymer to form various BP/EC blends. These blends exhibit competitive hydrogen-bonding interaction phenomena, which were analyzed using one-dimensional and two-dimensional FTIR analyses. Interestingly, after thermal treatment of BP/EC blends at 150 °C, the ordered self-assembled lamellae or hexagonal packed cylinder structures transform into the disordered micelle or disorder structure in BP/EC blends as a result of the transesterification reaction due to EC becoming miscible with a VBAZ-BZ-2OH monomer, disrupting the ordered self-assembled structure, which was confirmed through TEM and SAXS analyses. The transesterification reaction could easily understand the order−disorder morphological transformation using BP/EC blends to replace thermogravimetric analysis (TGA) coupled with microcomputed gas chromatography (TGA-GC) analyses.
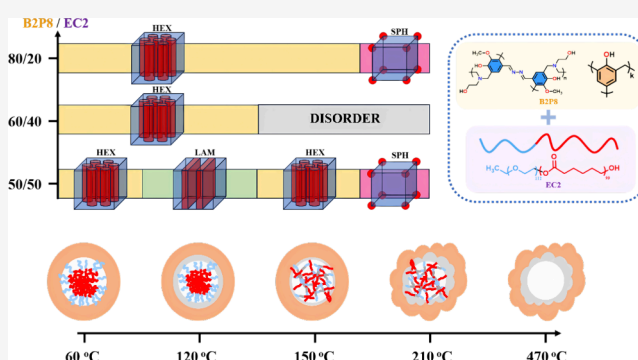
INTRODUCTION

Recent studies have highlighted vanillin's significant potential in biomaterial applications due to its biocompatibility and biodegradability.[1−15] As an ideal candidate for creating resin materials from natural sources, vanillin can be modified to produce high-molecular-weight materials with excellent mechanical properties and thermal stability.[3−6] Its versatility allows it to replace conventional petroleum-based resins in various applications, reducing the environmental impact. Moreover, using vanillin aligns with green chemistry principles and promotes the development of sustainable materials.[7−18] Therefore, utilizing vanillin as a resin material is technically feasible and offers considerable environmental and economic benefits.

Phenolic resin, also known as phenol-formaldehyde resin, is highly effective as a reinforcing cross-linked material in various composite applications. The reaction between phenol and formaldehyde creates a densely cross-linked polymer network, significantly enhancing the structural integrity and durability of polymeric materials.[19−22] Polybenzoxazines (PBZs) are an advanced class of phenolic resins, distinguished by their

exceptional properties and the ease of their synthesis through the thermal polymerization of benzoxazine monomers.[23−30] Unlike many other polymers, PBZs do not require catalysts for their formation, significantly enhancing their appeal for various industrial applications. Their remarkable attributes, such as high thermal stability,[18,26] robust mechanical properties,[10] chemical resistances,[21] low flammability,[11−13] low surface free energy,[14,29] and adaptability in nitrogen content adjustment, highlight their potential in numerous high-tech and industrial domains. PBZs represent the next generation of high-performance polymers, merging simplicity of the synthesis with a suite of desirable properties for advanced material applications. These characteristics render PBZs ideal for high-performance uses, including CO$_2$ adsorbents,[15,30−33] battery

Scheme 1. Phase Separation Behavior of VBAZ-BZ-2OH/BP/EC Diblock Copolymers under Varying Temperature Conditions
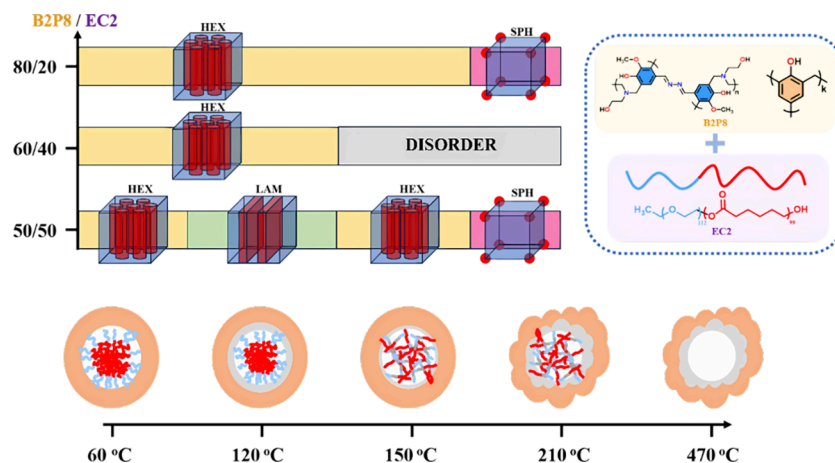
cathodes,[16,30,34] electronic components,[35,36] coatings,[17,18,27,37] and aerospace materials.[38,39]

In recent decades, there has been a substantial amount of research focused on the microphase separation phenomenon in diblock copolymers.[40−45] These diblock copolymers possess inherent thermodynamic properties that enable the self-assembly of a diverse array of nanostructures.[41] The structures formed by diblock copolymers include lamellae (LAM), hexagonal packing cylinders (HPC), spheres, double gyroids (DG), and specialized Frank-Kasper phases,[43,46−48] which are predominantly influenced by the volume fraction, interaction parameter (χ), and degree of polymerization (N) of block copolymers.[49−56] They have garnered widespread attention for applications in soft lithography,[57] photonic crystals,[58] nanocomposites,[59] and mesoporous materials.[60,61] Building on this foundation, we aim to utilize diblock copolymers to facilitate reaction-induced microphase separation (RIMPS) and this technique induces phase separation by initiating a chemical reaction within the copolymer system to form specific nanostructures with phenolic or PBZ resins.[54,56] The primary advantage of the RIMPS technique lies in its precise control over the process and outcome of phase separation, thereby achieving specific material properties and meeting application requirements. This method holds significant potential for fields such as nanomanufacturing,[41] functional materials,[62,63] and advanced material design.[64−66] Over the past two decades, we have delved into the use of block copolymers combined with phenolic or PBZ resins to examine the influence of hydrogen-bonding strength within these systems,[65,66] including PEO-*b*-PBLG,[51] PEO-*b*-PCL,[52,55] and PEO-*b*-PLA block copolymers.[53] Our findings indicate that as the temperature rises, the formation and dissociation of hydrogen bonds significantly impact the microphase separation structure,[67] enabling precise control over the microstructure and ultimate properties of the materials. In recent years, we also have incorporated inorganic hybrids into phenolic resin systems to observe the FK phase by increasing the χ value.[46,48]

Transesterification is a chemical process involving the exchange of organic groups between an ester and alcohol, typically catalyzed by a Lewis acid or base, resulting in the formation of a new ester and new alcohol.[68] This process is pivotal in various industrial applications, such as biodiesel production,[69−71] polymer synthesis,[71] and the modification of oils and fats. This study delves into the transesterification reaction mechanism, with a particular emphasis on the

utilization of Lewis bases as catalysts.[72,73] These Lewis bases facilitate the transesterification reaction by interacting with the carbonyl carbon of the ester. The lone pair electrons of the Lewis bases enhance the nucleophilic attack of the alcohol on C=O of the ester, thereby accelerating the reaction and leading to the formation of novel ester structures. Verge et al. developed a self-catalytic method to polymerize and transesterify various benzoxazine monomers in the existence of aliphatic hydroxyl (OH) units.[68] TGA coupled with TGA-GC analyses provided evidence of a transesterification reaction due to the hydroxyl groups with the tertiary amine groups, and the rate of methanol release was also investigated by different temperature treatments. The result reveals a temperature above 150 °C, the methanol is indeed released because of the transesterification reaction.[68] Based on this reason, the observation of transesterification reaction in the benzoxazine monomer by using another characterization such as SAXS and TEM image is also important recently.

Vanillin, a naturally derived and renewable compound, was selected as the starting material for this synthesis due to its sustainability and suitability for benzoxazine chemistry.[74] Benzoxazine derivatives synthesized from vanillin are known to possess advantageous characteristics, including a low exothermic curing peak, making them highly desirable for various practical applications.[74] The primary aim of this study was to design and synthesize bio-based molecules containing hydroxyl functional groups, such as VBAZ-BZ-2OH, to enable hydrogen-bonding interactions with PEO-*b*-PCL diblock copolymers. These hydrogen-bonding interactions are integral to inducing and regulating the phase separation within the system. By leveraging the specificity and strength of these interactions, the study seeks to gain deeper insights into the mechanisms governing phase separation and to explore its impact on the structural and material properties of the system.

Therefore, a difunctionalized bio-based vanillin azine monomer, known as VBAZ-2OH, was synthesized by reacting vanillin with $NH_2NH_2 \cdot H_2O$ through a Schiff base reaction in this study. Subsequently, using 1,4-dioxane as the solvent, we synthesized a novel VBAZ-BZ-2OH, through a Mannich condensation reaction involving VBAZ-2OH, ethanolamine, and $(CH_2O)_n$. We then investigated the phase behavior of blends comprising VBAZ-BZ-2OH/phenolic resin (BP) with varying weight ratios with PEO-*b*-PCL (EC) diblock copolymers. FTIR is utilized to identify the competitive hydrogen-bonding interactions within the BP/EC blends. The
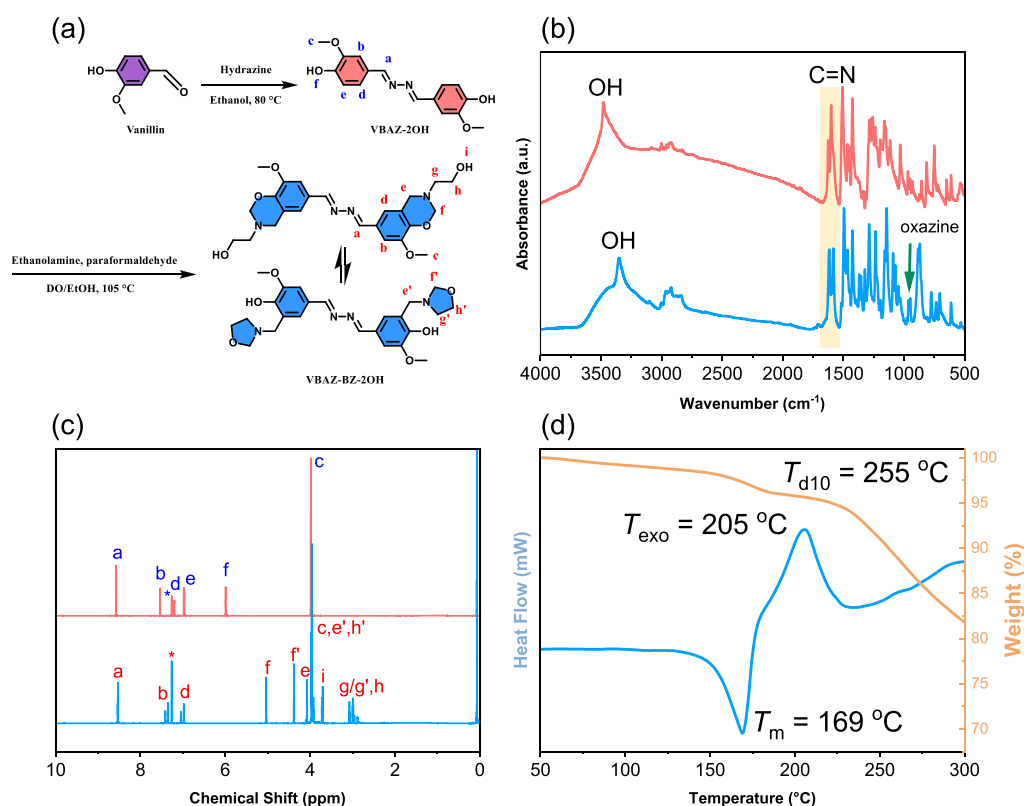
Figure 1. (a) Synthesis of VBAZ-BZ-2OH and the corresponding (b) FTIR spectrum, (c) ^{1}H NMR analysis (* is the peak for chloroform-*d*), and (d) TGA and DSC profiles of VBAZ-BZ-2OH.

Scheme 2. Transformation between the β-Amino-Alcohol Derivative of Benzoxazine and Oxazolidine Structures
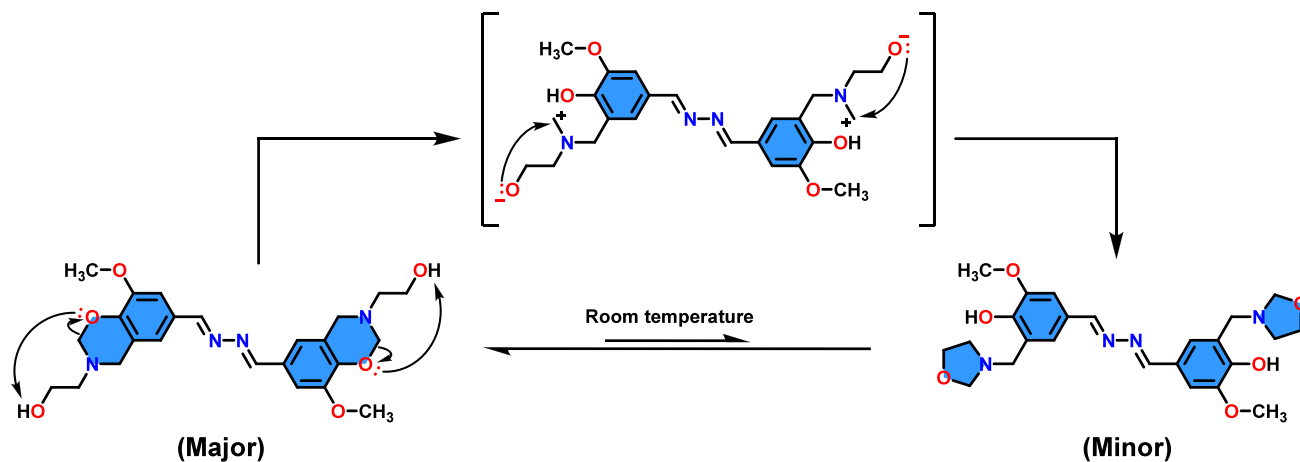
thermal properties are assessed using DSC and TGA. Following the thermal treatment, SAXS analysis is employed to map the self-assembled structure phase diagram, and TEM images offer insights into the local self-assembled microstructure. This comprehensive approach enables us to monitor the order−disorder morphological phase transitions of the system upon thermal heating. Notably, after heating the BP/EC blends at 150 °C, the ordered phase in the B2P8/EC = 60/40 blends transitions into a disordered micelle phase. This change occurs because EC becomes miscible with VBAZ-BZ-2OH, disrupting the ordered structures and implying the transesterification reaction occurring. Scheme 1 illustrates the microphase separation behavior of VBAZ-BZ-2OH/BP with

varying weight ratios when combined with EC diblock copolymers, observed at different temperatures.

■ EXPERIMENTAL SECTION

Materials. Toluene (99%), tin(II) 2-ethylhexanoate (96%), hydrochloric acid (HCl), vanillin (99%), paraformaldehyde (CH$_2$O)$_n$, hydrazine monohydrate (NH$_2$NH$_2$.H$_2$O, 98%), ε-caprolactone (99%), 1,4-dioxane (DO, 97%), and ethanol (99.5%) were procured from Alfa Aesar. Magnesium sulfate anhydrous (99%), phenol (100%), and NaOH (97%) were procured from SHOWA. Poly(ethylene glycol)methyl ether [PEO$_{112}$, M_n = 5000 g/mol] was procured from Sigma-Aldrich. Ethanolamine (99%) was procured from ACROS. The synthesis of resol-type phenolic resin was prepared according to previous studies.[46,48,75,76] PEO-*b*-PCL with various lengths was constructed through ring-opening polymerization (ROP)
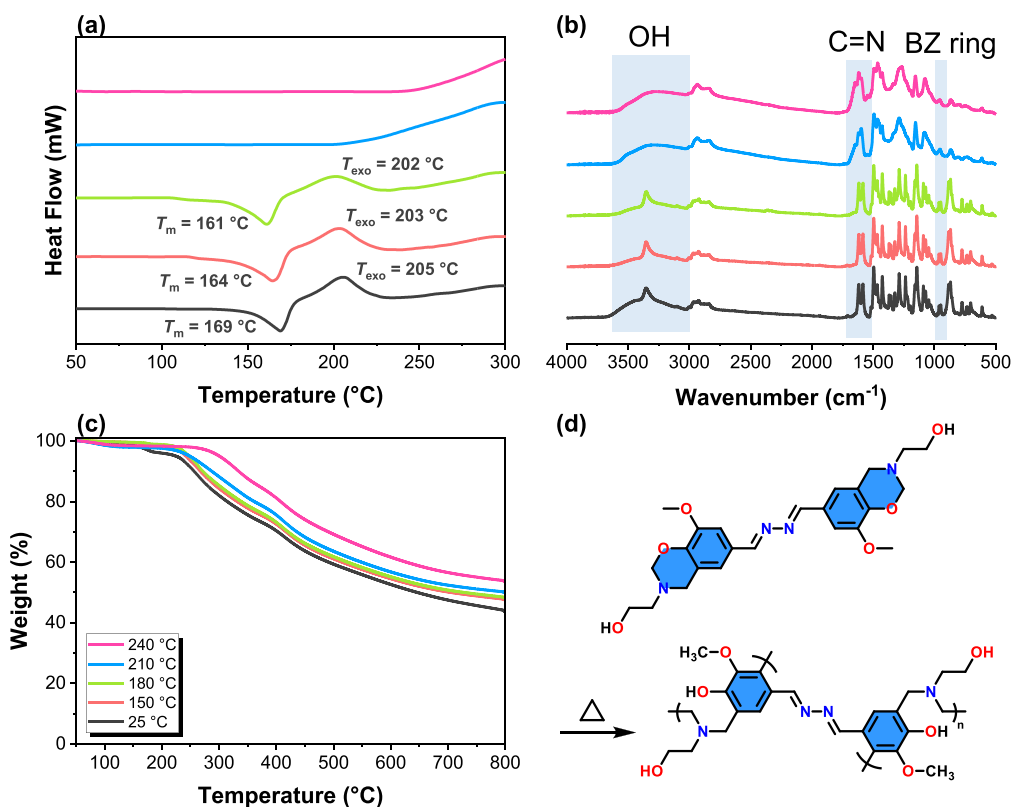
Figure 2. (a) Dynamic DSC profiles, (b) FTIR spectra, and (c) TGA profiles of VBAZ-BZ-2OH, along with (d) the possible molecular structure of VBAZ-BZ-2OH after ROP of the oxazine units.
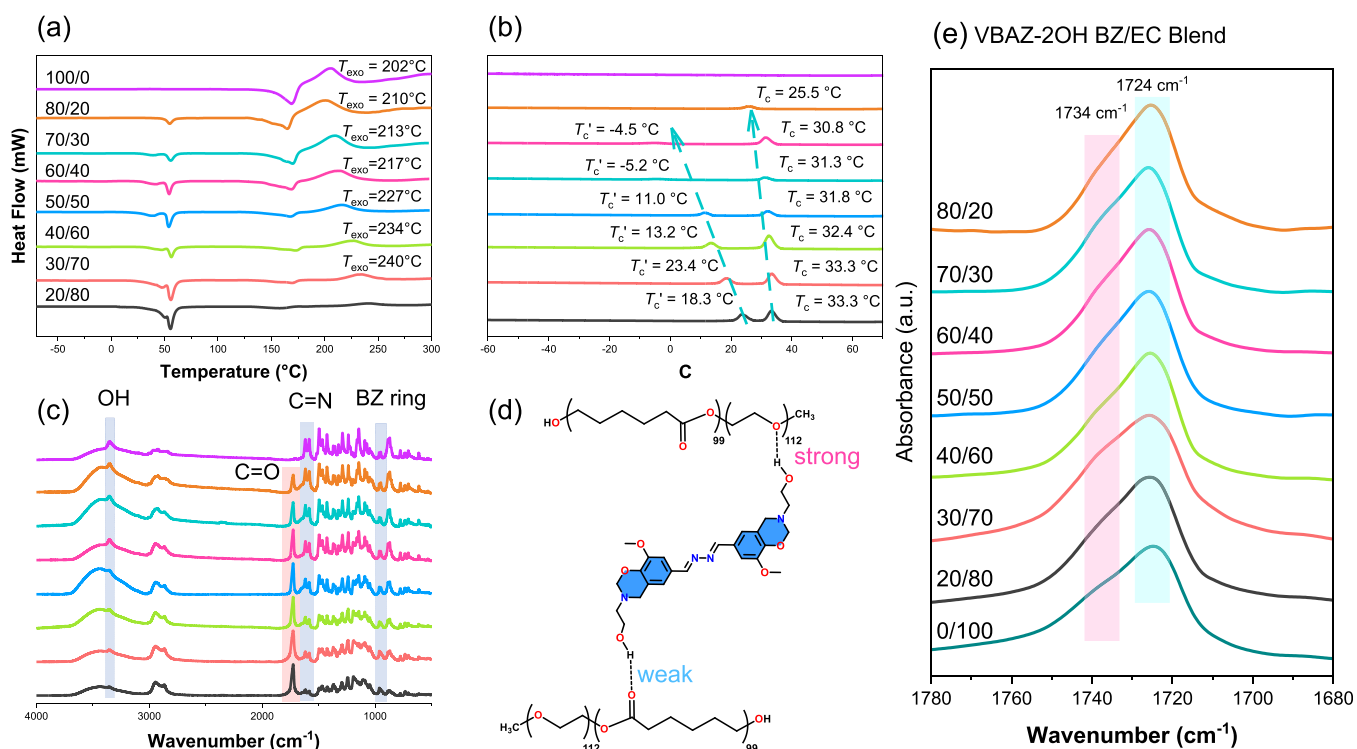
Figure 3. DSC thermograms of the VBAZ-BZ-2OH/EC blend with diverse compositions: (a) first heating cycle and (b) first cooling cycle; (c) FTIR spectra of VBAZ-BZ-2OH/EC blends, (d) illustration of hydrogen bonding between EC and VBAZ-BZ-2OH at 25 °C, and (e) FTIR spectra showing C=O groups in the VBAZ-BZ-2OH/EC blend at 25 °C.

following the methodology described in prior studies [Scheme S1].[46,48,77] The molecular weights and polydispersity index (PDI)

of the synthesized different kinds of PEO-*b*-PCL through ROP are provided in Table S1.
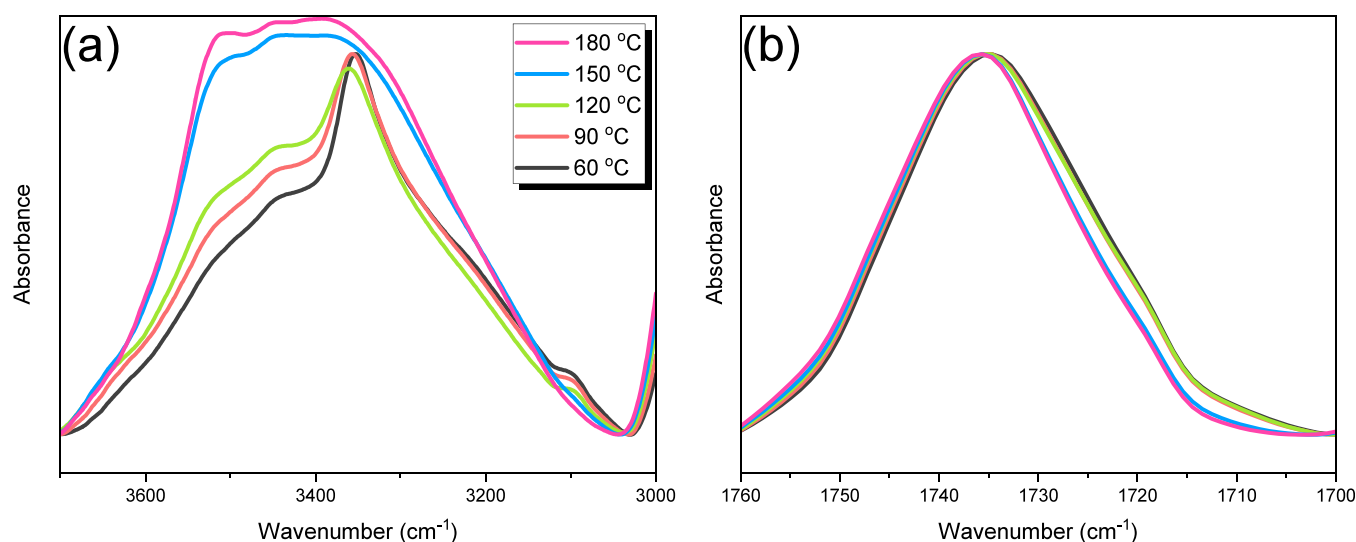
Figure 4. FTIR spectra illustrating (a) the O−H groups and (b) the C=O groups of the VBAZ-BZ-2OH/EC = 60/40 blend, recorded at different temperatures.

Scheme 3. Possible Transesterification Reactions between VBAZ-BZ-2OH and EC
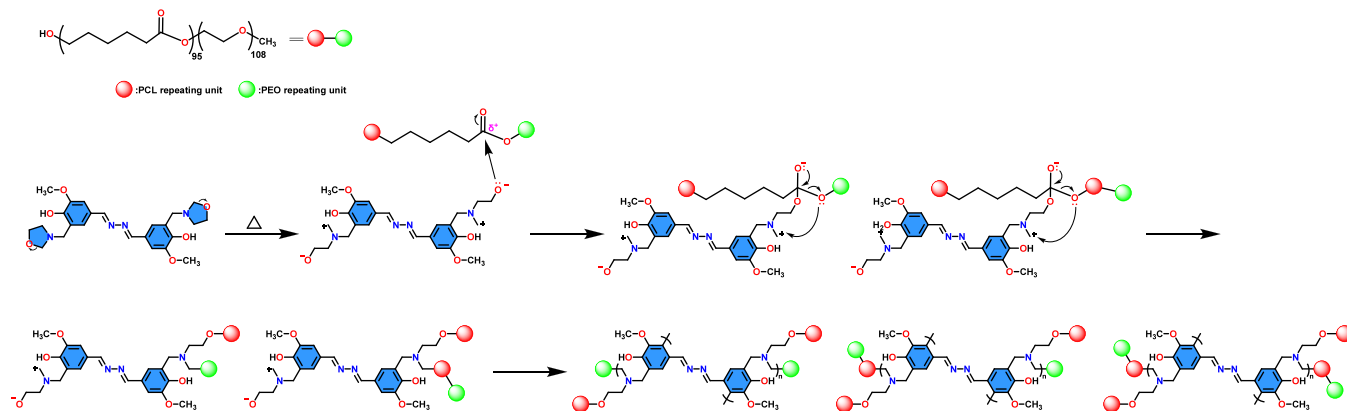
Synthesis of VBAZ-2OH. Under a nitrogen atmosphere, 9.97 g (65.5 mmol) of vanillin and 1.05 mL (32.8 mmol) of hydrazine monohydrate were added to 50 mL of ethanol and then the reaction proceeded for 24 h at 25 °C. The solid was then filtered and washed with ethanol, yielding 9.52 g (31.7 mmol) of a light-yellow solid, with a high yield of 96.8%.

Synthesis of VBAZ-BZ-2OH. In a 100 mL flask under a nitrogen atmosphere, $(CH_2O)_n$ (3.60 g, 119.8 mmol), VBAZ-2OH (9.00 g, 30.0 mmol), and ethanolamine (3.62 mL, 60.0 mmol) in 100 mL of DO were mixed. The mixture was kept at 100 °C for the entire day. Subsequently, the solution was concentrated by using a rotary evaporator to yield a yellow solid. This solid was further washed three times with ethanol to obtain an amber-colored solid (14.10 g, yield: 93%).

Preparation of VBAZ-BZ-2OH/EC Blends. VBAZ-BZ-2OH and EC in varying ratios were prepared. THF was used to dissolve the VBAZ-BZ-2OH/EC blends, after which the solutions were transferred to an aluminum pan. To conduct the evaporation-induced self-assembly (EISA) process, the solvent progressively evaporated for 36 h at 35 °C.

Preparation of VBAZ-BZ-2OH/Phenolic/EC [BP/EC]. Blends of VBAZ-BZ-2OH, phenolic resin, and EC in varying ratios were prepared. Specifically, the weight ratios of VBAZ-BZ-2OH to phenolic resin were set at 20/80 and 40/60, abbreviated as B2P8 and B4P6, respectively. THF was utilized to dissolve the B2P8/EC and B4P6/EC blends, and the resulting solutions were transferred to aluminum pans. The solvent was gradually evaporated at 35 °C over 36 h to

complete the EISA process. The resulting material was then solidified through a pyrolysis procedure, which involved heating the mixture for 4 h at 150 °C, followed by 10 h at 210 °C, to facilitate cross-linking of benzoxazine and phenolic resins. Subsequently, the mixtures were subjected to further heating for 5 h at temperatures exceeding the pyrolysis threshold of 470 °C, leading to the formation of mesoporous BP materials.

■ RESULTS AND DISCUSSION

Synthesis and Characterization of the VBAZ-BZ-2OH Monomer. The synthesis of the VBAZ-BZ-2OH monomer is carried out via a Mannich condensation reaction involving VBAZ-2OH, $(CH_2O)_n$, and ethanolamine, as depicted in Figure 1a. The chemical structure and properties of synthesized VBAZ-BZ-2OH were verified using various analytical methods, including FTIR, ^1H NMR, TGA, and DSC. FTIR analyses for VBAZ-2OH and VBAZ-BZ-2OH monomers [Figure 1b] revealed a prominent peak at 3352 cm^{-1}, indicative of OH stretching. Absorption peaks at 3004 and 3101 cm^{-1} were attributed to sp^2-hybridized C−H stretching, while those at 2923, 2946, and 2965 cm^{-1} were assigned to sp^3-hybridized C−H bonds. The presence of the vanillinazine structure was confirmed by the imine bond signals at 1617 cm^{-1} (asymmetric) and 1583 cm^{-1} (symmetric). After the Mannich condensation reaction, oxazine ring formation
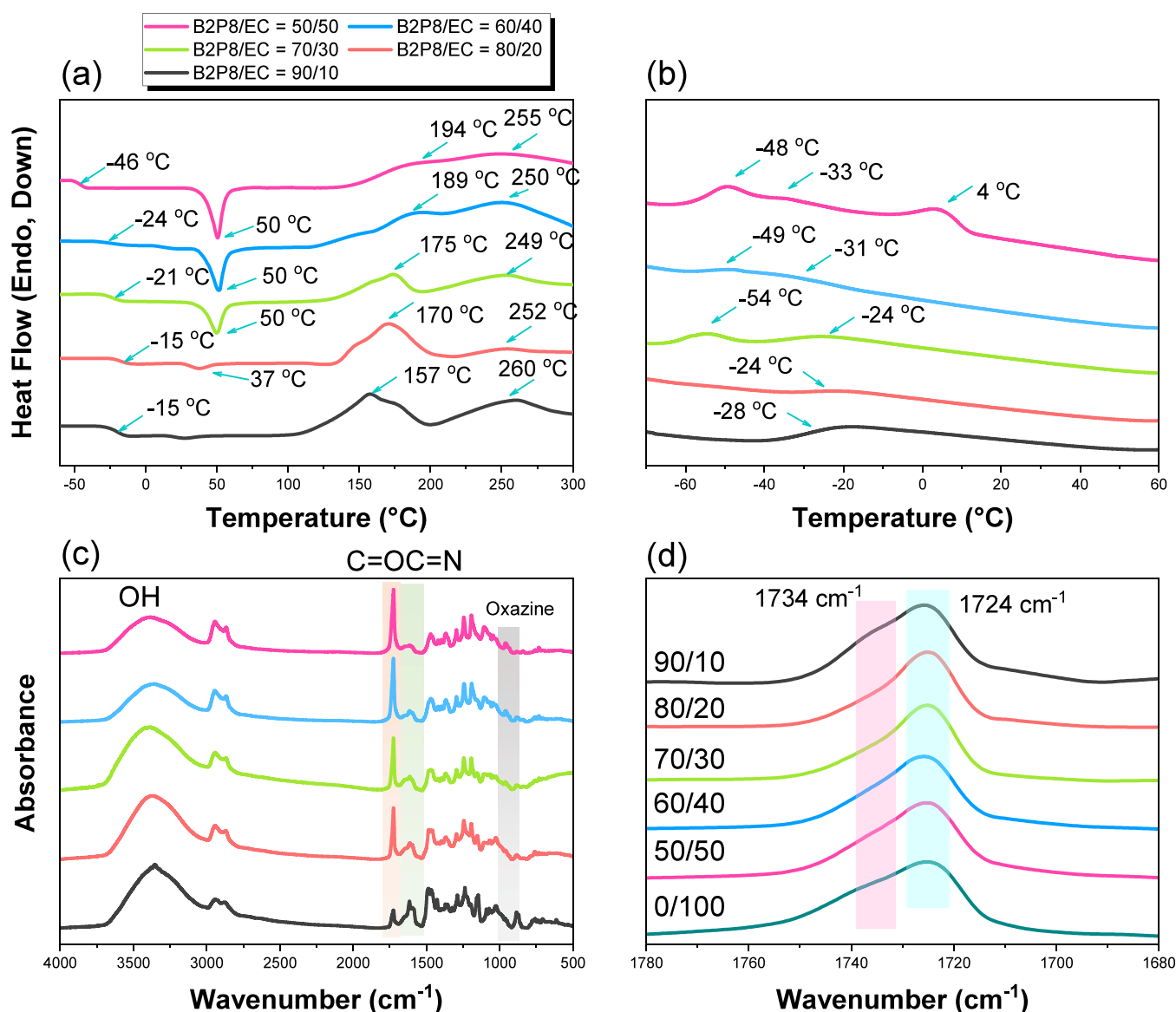
Figure 5. DSC thermograms of B2P8/EC = 50/50 to 90/10 blends of various compositions: (a) second run of heating state and (b) first run of cooling state; (c) FTIR of B4P6/EC blends and (d) FTIR of C=O units of the B4P6/EC blend at 25 °C.

was indicated by absorption peaks at 949 cm⁻¹ in the VBAZ-BZ-2OH structure, as shown in Figure 1b. Figure 1c presents the distinct singlet peaks of VBAZ-2OH at 8.57 ppm (a), 7.53 ppm (b), 5.99 ppm (f), and 3.98 ppm (c), corresponding to the protons of N=C−H, aromatic C−H, O−H group, and OCH₃ groups.[78,79] Furthermore, VBAZ-2OH displayed doublets of doublet peaks for the aromatic C−H group at 7.21−7.20 ppm (d) and 6.98−6.96 ppm (e). Following the Mannich condensation reaction, the absence of a signal for the OH groups of VBAZ-2OH and the formation of the oxazine ring in VBAZ-BZ-2OH was confirmed by singlet peaks at 5.03 ppm (f) and 4.07 ppm (e), which matched the O−**CH₂**−N and Ar−**CH₂**−N units, respectively.

Additionally, peaks for the oxazolidine structure identified the singlet peaks at 4.38 ppm (f′) and 3.97 ppm (e′) and triplet peaks at 3.92 ppm (h′), and in Figure S1, the carbon signals of the vanillinazine structure were detected in the range of 110−165 ppm.[68] Peaks at 8.53, 6.98−7.41, 3.70, 3.07, and 2.99 ppm were attributed to the protons of N=C−H, aromatic C−H, OCH₃, OH group, and β-amino-alcohol group units,

respectively. In Figure S2, the oxazine ring is identifiable at 49.5 and 83.8 ppm, while the oxazolidine structure can be distinguished at 53.4 and 85.7 ppm, respectively. Scheme 2 illustrates the potential formation of oxazolidine-based structures from the β-amino-alcohol adduct. Based on ¹H NMR spectrum analysis, the fraction values of benzoxazine and oxazolidine structures are 62.11 and 37.89%, respectively. Moreover, DSC and TGA analyses of the uncured VBAZ-BZ-2OH monomer revealed a melting point at 169 °C and a thermal ring-opening polymerization (ROP) reaction at 205 °C, with a thermal decomposition temperature (T_{d10}) of 255 °C, as shown in Figure 1d.

Figures 2a and 2b present the DSC profiles and FTIR spectra, respectively, of VBAZ-BZ-2OH under various thermal treatment conditions. Before the thermal treatment, we could observe a melting point at 169 °C and an exothermic curing point at 205 °C for VBAZ-BZ-2OH. As the thermal treatment temperature escalated from 25 to 180 °C, both the melting point and thermal curing peaks of the BZ ring shifted to lower temperatures. When the temperature was further escalated
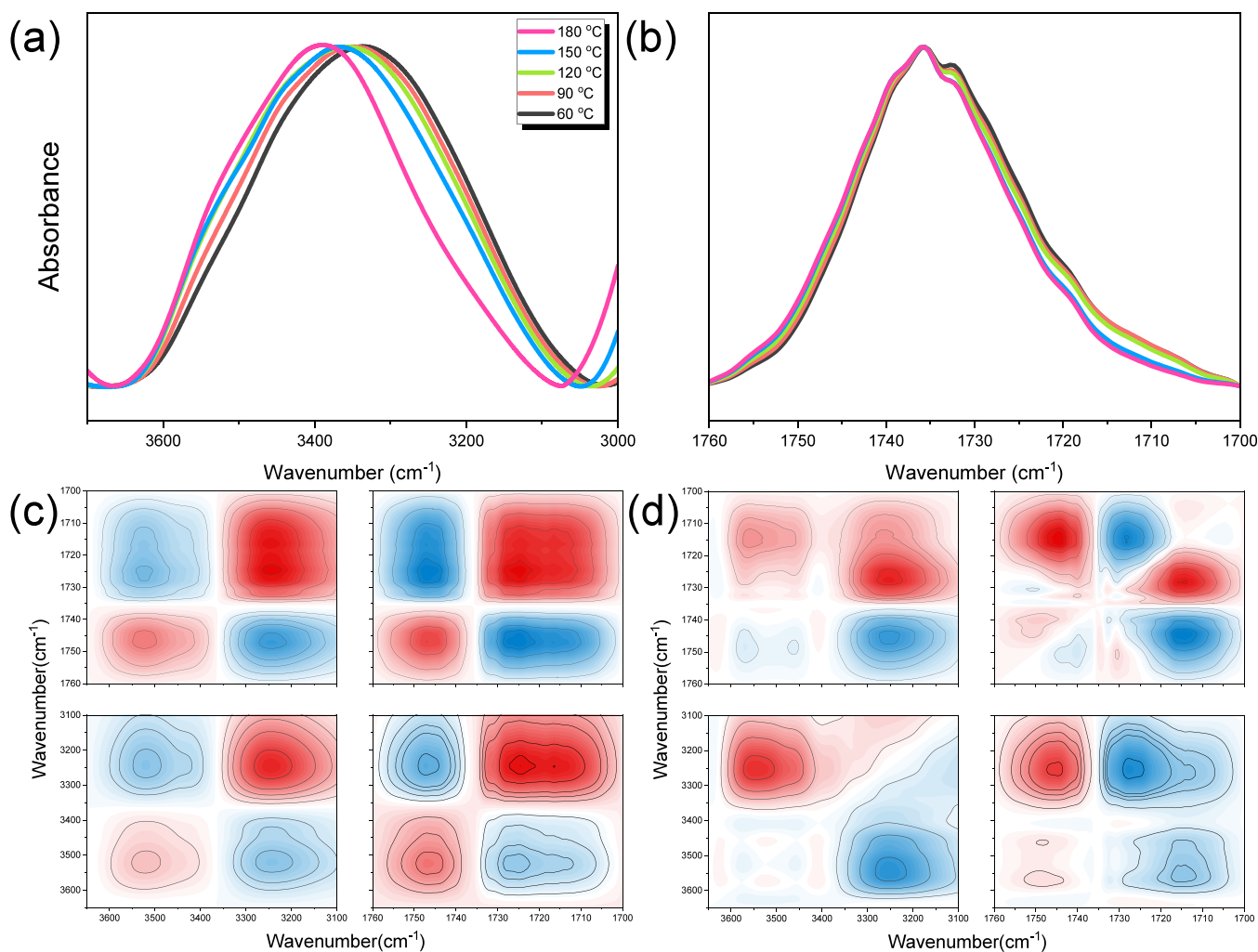
Figure 6. FTIR spectra showing (a) O−H groups and (b) C=O groups of the B2P8/EC = 60/40 blend, recorded at diverse temperatures; corresponding 2D FTIR spectra: (c) synchronous and (d) asynchronous correlation maps.

from 210 to 240 °C, the thermal ROP peaks completely disappeared, indicating the formation of a highly cross-linked poly(VBAZ-BZ-2OH) network, as illustrated in Figures 2a,d. Additionally, Scheme S2 outlines the potential thermal polymerization mechanism of VBAZ-BZ-2OH at elevated temperatures. Concurrently, Figure 2b shows that the absorption bands of the oxazine ring at 949 cm^{-1} diminished as the thermal curing temperature rose from 25 to 180 °C and completely vanished after 210 °C, consistent with the DSC results shown in Figure 2a. Figure 2c provides TGA analyses, revealing that the untreated VBAZ-BZ-2OH monomer exhibited a T_{d10} of 255 °C and a char yield of 43 wt %. Following thermal treatment, the T_{d10} values escalated moderately to 267, 271, 286, and 334 °C, with corresponding char yields of 47, 48, 50, and 53 wt %, as evidenced in Figure 2c and the data are summarized in Figure S3, respectively.

Preparation and Characterization of VBAZ-BZ-2OH/EC Blends. Previous studies investigated the hydrogen-bonding interactions between phenolic OH and the ether group (C−O−C) of PEO repeating units, as well as the C=O units of the PCL block.[76] In our current research, we synthesized different molecular weight copolymers of PEO-*b*-PCL and their structures confirmed by FTIR and ^{1}H NMR analyses, as illustrated in Figure S4. Briefly, the absorption bands for all synthesized EC with varying molecular structures

are centered at 3452, 1724, and 1046 cm^{-1}, corresponding to the presence of OH, C=O, and C−O−C units, respectively [Figure S4a]. Furthermore, the ^{1}H NMR spectra [Figure S4b] of all synthesized EC revealed proton signals at 4.05, 3.65, 2.31, and 1.65 ppm, which correspond to the OC=O**CH₂**, O**CH₃**, **CH₂**OH, and OC=OCH₂**CH₂**CH₂ groups, respectively. Figure S5 presents the DOSY spectrum of PEO$_{112}$-*b*-PCL$_{99}$, and the diffusion coefficient is quantified at $D = 2.34 \times 10^{-10}$ m^2 s^{-1}. Specifically, we selected PEO$_{112}$-*b*-PCL$_{99}$ for the blend with VBAZ-BZ-2OH.

We initially prepared blends of various ratios of VBAZ-BZ-2OH/EC for FTIR, TGA, and DSC analyses, as shown in Figure 3a−c and Figure S6. As the proportion of VBAZ-BZ-2OH escalates, the char yield of VBAZ-BZ-2OH/EC also rises. We summarize the T_{d10} values and char yields for various VBAZ-BZ-2OH/EC blend ratios in Figure S7. The DSC thermograms from the cooling thermograms indicated that the crystallization temperatures (T_c and T_c') shifted to higher temperatures as the proportion of VBAZ-BZ-2OH decreased, while the heating thermograms exhibited endothermic melting temperatures around 55 °C for EC and 169 °C for VBAZ-BZ-2OH. The exothermic curing temperature escalated from 202 to 240 °C, as depicted in Figure 3a,b and Table S2. The second cooling cycles of VBAZ-BZ-2OH/EC = 50/50 revealed
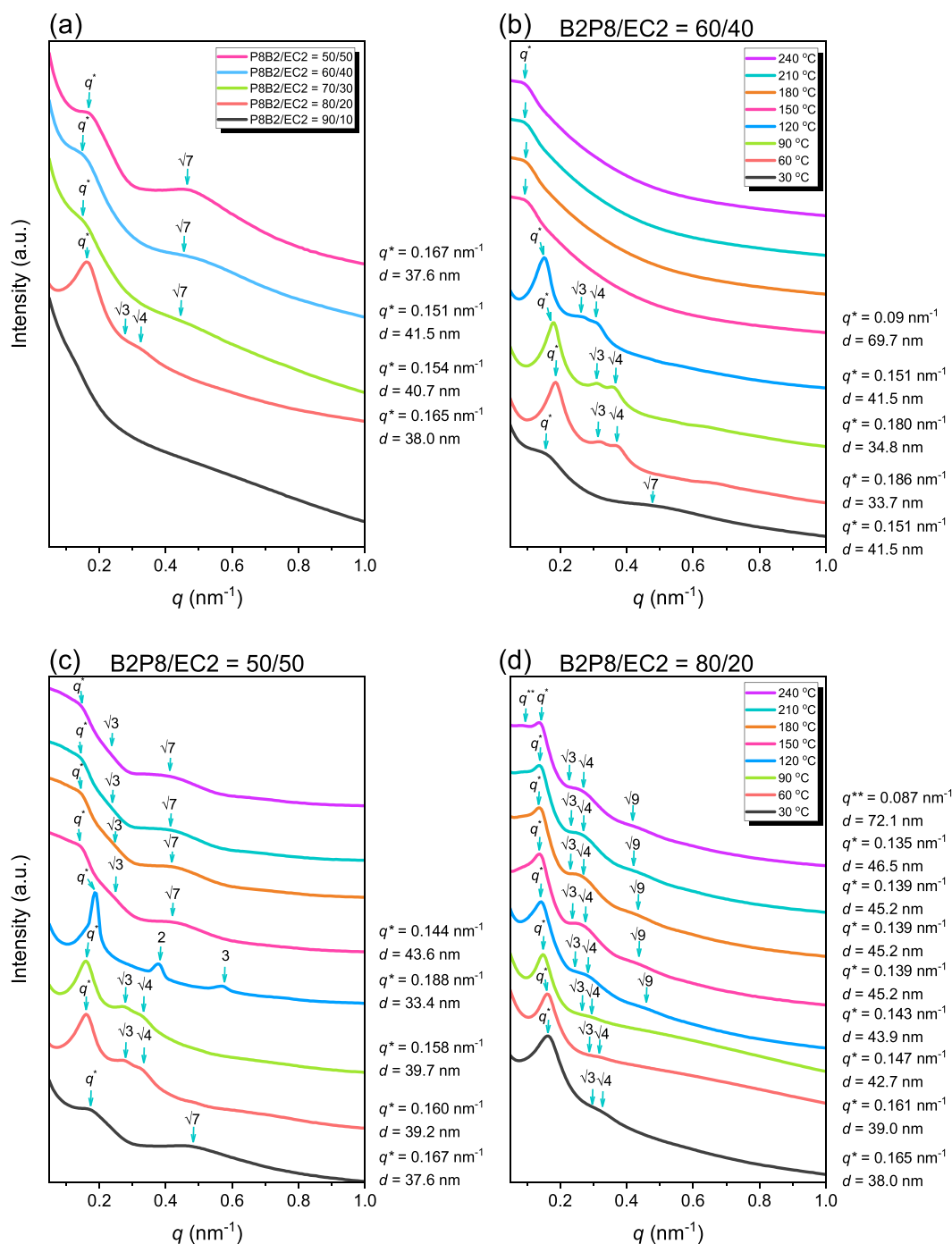
Figure 7. SAXS patterns for (a) B2P8/EC = 50/50 to 90/10 at 25 °C; (b) B2P8/EC = 60/40, (c) B2P8/EC = 50/50, and (d) B2P8/EC = 80/20 of SAXS patterns during different temperatures.

the crystallization temperatures shifted to higher temperatures at 19 and 33 °C, while the heating cycles of VBAZ-BZ-2OH/EC = 50/50 revealed endothermic melting temperatures at 53 °C, and the exothermic curing temperature vanished in Figure S8. As shown in Table S2, increasing the proportion of VBAZ-BZ-2OH had a minimal effect on the melting point (T_m) of the PEO segment, which remained at approximately 55 °C. However, the T_c of the PEO segment decreased from 33.3 to 25.5 °C, attributed to strong hydrogen-bonding interactions. In contrast, the melting point (T_m') of the PCL segment dropped significantly from 50.7 to 39.5 °C, while its T_c' decreased markedly from 18.3 to −4.5 °C. The FTIR spectra of various

VBAZ-BZ-2OH/EC blend ratios revealed an increase in the imine bond peaks (at 1583 and 1618 cm^{-1}) and the oxazine ring peak (at 950 cm^{-1}), whereas the carbonyl bond peak (at 1724 cm^{-1}) decreased with the escalating proportion of VBAZ-BZ-2OH, as shown in Figure 3c. Figure 3d highlights the robust hydrogen-bonding interactions between the OH groups of VBAZ-BZ-2OH and the ether groups of the PEO segment in EC, along with a weaker interaction between the OH groups of VBAZ-BZ-2OH and the C=O groups of the PCL segment in EC, corresponding to Figure 3e. Figure 3e delineates the free carbonyl (C=O) groups in the PCL segment of the blends and pure EC, distinguishing the amorphous regions at 1734 cm^{-1}
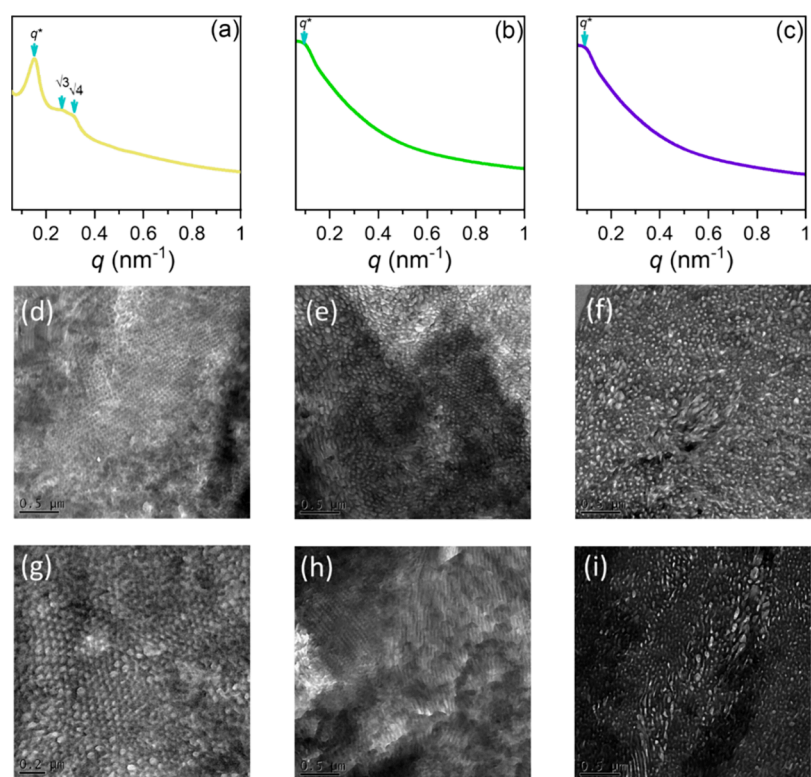
Figure 8. SAXS patterns of the B2P8/EC blend in a 60/40 ratio at (a) 120 °C, (b) 150 °C, and (c) 210 °C, along with the corresponding TEM images at 120 °C (d, g), 150 °C (e, h), and 210 °C (f, i).
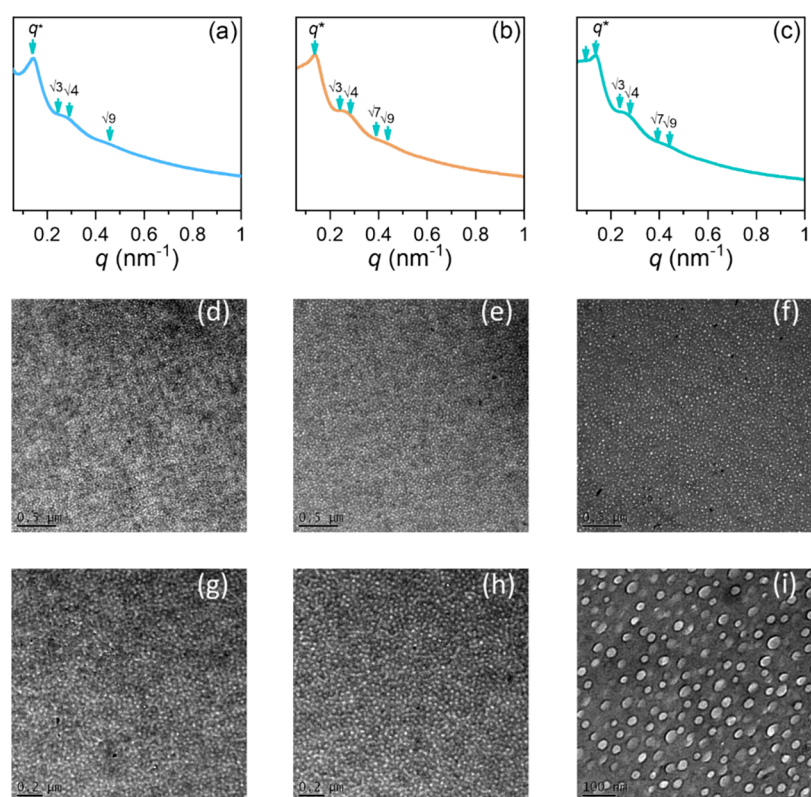
Figure 9. SAXS patterns of the B2P8/EC blend in the 80/20 ratio at (a) 120 °C, (b) 150 °C, and (c) 210 °C, along with the corresponding TEM images at 120 °C (d, g), 150 °C (e, h), and 210 °C (f, i).

and crystalline regions at 1724 cm^{-1}.[43,48,56] Furthermore, the VBAZ-BZ-2OH/EC = 60/40 blends exhibited single diffusion,

indicating hydrogen-bonding interactions between VBAZ-BZ-2OH and EC, as shown in Figure S9. Figure S10 illustrates the
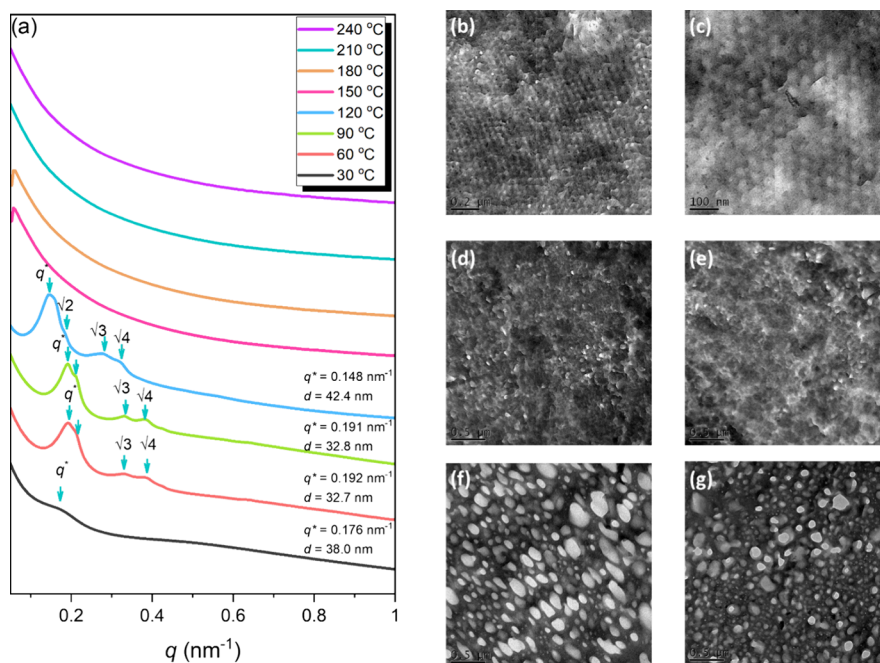
Figure 10. SAXS patterns of B4P6/EC = 60/40 at (a) 120 °C, (b) 150 °C, and (c) 210 °C and the corresponding TEM images at 120 °C (b, c), 150 °C (d, e), and 210 °C (f, g).
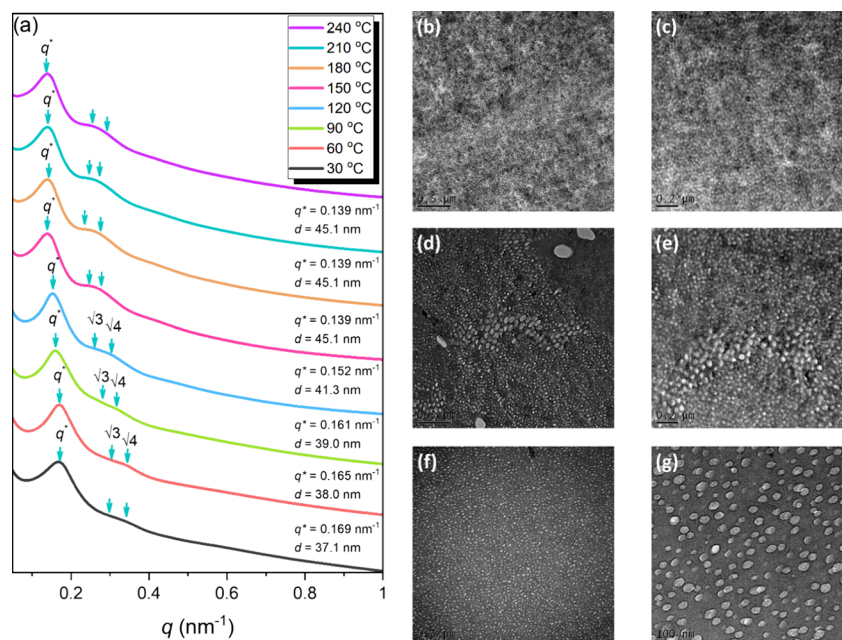
Figure 11. SAXS patterns of B4P6/EC = 80/20 at (a) 120 °C, (b) 150 °C, and (c) 210 °C and the corresponding TEM images at 120 °C (b, c), 150 °C (d, e), and 210 °C (f, g).

C−O−C groups in the PEO segment of the blends and pure EC, highlighting the amorphous peaks at 1244 cm^{-1} and the crystalline peaks at 1192 cm^{-1}. As the proportion of VBAZ-BZ-2OH escalated, a new peak appeared at 1236 cm^{-1}, signifying that the C−O−C stretch was affected by hydrogen bonding.

We recorded temperature-dependent FTIR spectra of VBAZ-BZ-2OH/EC = 60/40 blends, as shown in Figure 4a,b and Figure S11. The FTIR spectra revealed that the peaks corresponding to OH groups shifted to higher wavenumbers from 60 to 120 °C, indicating a decrease in hydrogen-bonded OH groups and an increase in free OH groups at 3514 cm^{-1}.

After reaching 150 °C, the OH bands became broader and the oxazine ring peak significantly diminished, as outlined in Figure 4a and Figure S11.

This phenomenon is attributed to transesterification reactions between VBAZ-BZ-2OH and EC, leading to the incorporation of EC into the VBAZ-BZ-2OH matrix, as illustrated in Scheme 3. Figure 4b and Figure S11 also show that the crystalline region of the C=O decreased substantially. In contrast, the amorphous region escalated significantly due to the melting of EC after 43 °C, as observed in Figure 3a and Table S2. The amorphous regions of the C=O groups shifted
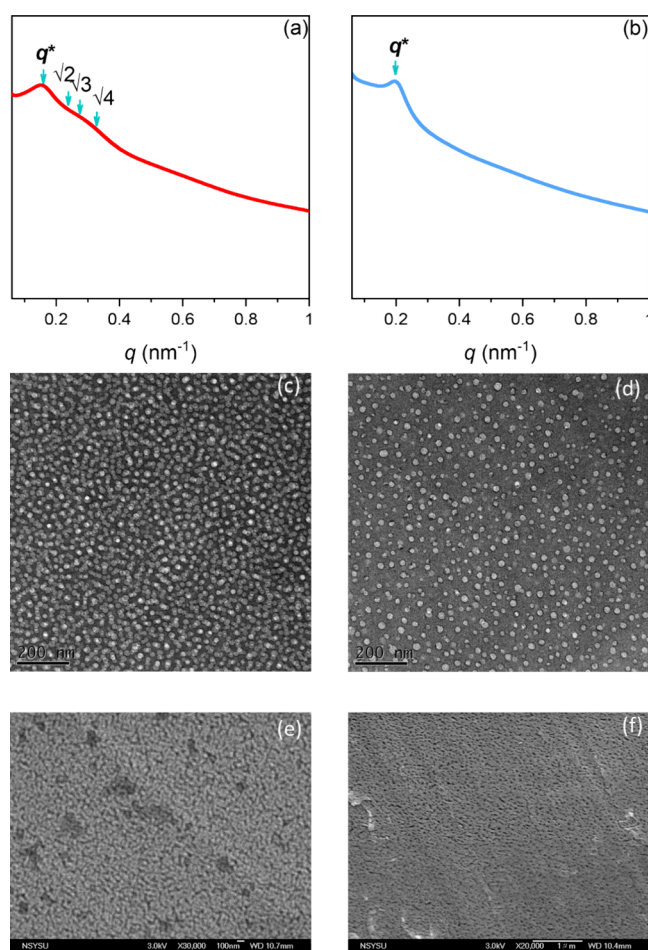
Figure 12. SAXS patterns, TEM, and SEM images of B4P6/EC = 80/20: (a, c, and e) and B2P8/EC = 80/20: (b, d, and f) after thermal pyrolysis at 470 °C.

to higher wavenumbers with escalating temperatures. In the VBAZ-BZ-2OH/EC blends, hydrogen-bonded carbonyl groups were scarcely observed. However, the hydrogen-bonded C−O−C group was detected at 1236 cm^{-1} and diminished with an escalating temperature, as shown in Figure S12. Consequently, there was weak competitive hydrogen-bonding interaction between VBAZ-BZ-2OH and EC, and microphase separation was hard to observe in Figure S13.

Characterization of VBAZ-BZ-2OH/Phenolic/EC Blends.

We prepared self-assembled blends with varying weight ratios of VBAZ-BZ-2OH/phenolic, specifically 20/80 and 40/60 (termed B2P8 and B4P6, respectively). The blends B2P8/EC were studied in ratios ranging from 50/50 to 90/10, as detailed in Figure 5a−c. In Figure 5a, the second heating cycle DSC thermograms reveal the glass-transition temperature (T_g) shifting from −15 to −46 °C. Figure 5b illustrates the exothermic curing temperature escalating from 157 to 194 °C, indicating that BP underwent thermal curing, as further supported by observations in Figure S14. Moreover, the second exothermic curing peak shifted to a higher temperature range of approximately 249−260 °C, suggesting that the residual VBAZ-BZ-2OH is influenced by the BP after cross-linking, causing the ROP reaction to occur at a higher temperature. The cooling thermograms from the first cycle, which correspond to Figure 5a, indicate that both T_c and T_g shifted to lower temperatures as the proportion of the EC

decreased. The FTIR spectra for various ratios of B2P8/EC blends reveal an increase in the imine bond peaks at 1615 cm^{-1} and the oxazine ring peak at 960 cm^{-1}, while the peak of the C=O groups at 1724 cm^{-1} diminished with the escalating proportion of B2P8, as illustrated in Figure 5c. Furthermore, Figure 5d details the decrease in the proportion of amorphous regions at 1734 cm^{-1} and the increase in the proportion of crystalline regions at 1724 cm^{-1}. This observation aligns with the shift in T_c (observed at 37 and 50 °C) of the PCL segment, as the proportion of EC decreased, as shown in Figure 5a. Additionally, Figure S15 illustrates the presence of free C−O−C groups within the PEO segment of the blends and pure EC, highlighting crystalline peaks at 1244 and 1192 cm^{-1}. As the proportion of VBAZ-BZ-2OH escalated, a new peak emerged at 1237 cm^{-1}, indicative of C−O−C stretching influenced by hydrogen bonding.

We conducted an in-depth FTIR analysis of the B2P8/EC = 60/40 blends as illustrated in Figure 6a,b and Figure S16. Our comprehensive observations revealed a noteworthy shift in the peaks corresponding to OH groups toward higher wavenumbers. This shift suggests a reduction in hydrogen-bonding OH groups and a concomitant increase in free OH groups, which become more pronounced at 3568 cm^{-1} with escalating temperatures. Figure 6b and Figure S16 further elucidate that as EC melts above 50 °C, there is a significant diminution in the crystalline region of carbonyl groups, while the amorphous region of carbonyl groups escalates notably, as detailed in Figure 5a. Specifically, the amorphous region of C=O units (at 1734 cm^{-1}) was diminished, whereas the presence of free C=O (at 1747 cm^{-1}) rose. The synchronous two-dimensional infrared (2D IR) correlation map between the carbonyl and OH groups is presented in Figure 6c. Our analysis reveals that the peaks for the free OH groups, located at 3568 cm^{-1}, and the hydrogen-bonding OH groups, situated between 3100 and 3500 cm^{-1}, exhibit a negative correlation. Similarly, the signal for free carbonyl units in the PCL is observed at 1747 cm^{-1}, and the hydrogen-bonding carbonyl units, located at 1715 cm^{-1}, also demonstrate a negative correlation, which is anticipated. Furthermore, we identified a significant correlation between the OH and carbonyl units. The peaks for free carbonyl units show a positive correlation with those of free OH units, while the peaks for hydrogen-bonding carbonyl units correlate positively with those of hydrogen-bonding OH units. Conversely, both peaks for hydrogen-bonding carbonyl units and hydrogen-bonding OH units exhibit a negative correlation with those of free carbonyl and OH units.

The asynchronous two-dimensional (2D) correlation map presented in Figure 6d exhibited a cross-peak between hydrogen bonding and free units. Specifically, this cross-peak was observed between OH units at 3568 and 3251 cm^{-1}, as well as between carbonyl units at 1747 and 1715 cm^{-1}, which were found to be negatively correlated. This observation is consistent with the behavior observed in the synchronous spectrum. Additionally, the lower right quadrant of Figure 6d indicates that the peaks at 3568 and 1747 cm^{-1} were positively correlated, whereas the peaks at 3251 and 1715 cm^{-1} were negatively correlated. The 2D maps further elucidate that the sequence of changes in intensity with escalating temperature followed a specific order: hydrogen-bonding carbonyl (C=O) at 1715 cm^{-1} > hydrogen-bonding OH at 3251 cm^{-1} > free carbonyl (C=O) at 1747 cm^{-1} > free OH at 3568 cm^{-1}. This sequence is logical because hydrogen-bonding interactions exhibit greater sensitivity to temperature increase compared to

free carbonyl groups, which contributes to a delayed response for free carbonyl groups. In conclusion, the strong hydrogen-bonding interactions present in the B2P8/EC blends are markedly distinct from those observed in the VBAZ-BZ-2OH/EC blends. Both the PEO and PCL blocks within B2P8 and EC display strong hydrogen-bonding forces. This results in competition between B2P8 and EC for these hydrogen bonds, ultimately leading to microphase separation.

Identification of Microphase Separation Transformation of B2P8/EC Blends. In our detailed examination of the self-assembled structures within the B2P8/EC blends at 25 °C, the SAXS patterns, as revealed in Figure 7a, provided highly insightful data. For the B2P8/EC blends with a composition ratio of 90/10, we identified disordered miscible structures.

These structures were indicated by the presence of a single T_g and higher levels of amorphous regions, as characterized by the carbonyl bond at 1734 cm^{-1}. Escalating the EC content to 20 wt % prompted the formation of short-range order cylinder structure, as reflected by a q^*/q ratio of $1:\sqrt{3}:\sqrt{4}$, as confirmed by the TEM image in Figure S17. This blend exhibited a single T_g and reduction in the carbonyl carbonyl regions. When the EC content was further escalated beyond 30 wt %, cylinder worm-like structures began to form, suggested by a q^*/q ratio of $1:\sqrt{7}$. Furthermore, the d-spacing values were calculated using Bragg's law ($d = 2\pi/q^*$), which revealed an increase in d-spacing as the EC proportion rose. Specifically, the d-spacing values escalated from 38.0 nm at 20 wt % EC to 41.5 nm at 40 wt % EC. This systematic analysis elucidates the structural transitions occurring within the B2P8/EC blends as a function of varying EC contents. Figure 7b illustrates that B2P8/EC blends with a 60/40 ratio exhibit a short-range order of cylinder worm-like structure with a d-spacing of 41.5 nm before thermal treatment. Notably, we observed that the blend underwent a phase transition from short-range order of cylinder worm-like structure to long-range order of hexagonal packed cylinder (HPC) structure, as indicated by a peak ratio shift to $1:\sqrt{3}:\sqrt{4}$ following thermal treatment at 60 °C. With further increases in the thermal treatment temperature, the q^* values decreased due to thermal expansion within the hexagonal structure, resulting in a shift to lower q values. At 120 °C, both the SAXS patterns and TEM images of this blend confirmed the presence of long-range order of HPC structure, as detailed in Figure 8a,d,g. When the temperature was elevated to 150 °C, Figure 8b,e,h indicates that the SAXS patterns and TEM images displayed a transition to a disordered structure. This change was attributed to transesterification reactions occurring between VBAZ-BZ-2OH and EC, causing EC to become miscible within the benzoxazine resins, as illustrated in Scheme 2. At 210 °C, the SAXS patterns and TEM images demonstrated that the blend retained a disordered spherical structure, as shown in Figure 8c,f,i. This comprehensive analysis elucidates the structural transitions within the B2P8/EC blends under varying thermal treatments, providing significant insights into the material's behavior and properties. This result provides the simple morphology change to identify transesterification reaction by using SAXS analyses to replace the TGA-GC analyses.[68]

Furthermore, the B2P8/EC blend with a 50/50 ratio initially demonstrated an d-spacing of 41.5 nm before any thermal treatment, as illustrated in Figure 7c. Similarly, the blend underwent its first phase transition from a sort of range order of cylinder worm-like structure to a long-range order of HPC structure, marked by a peak ratio shift to $1:\sqrt{3}:\sqrt{4}$ after

thermal treatment at 60 °C. According to thermodynamic theory, a reduction in interfacial energy prompts self-assembling micelles to expand their interfacial surface area to minimize Gibbs free energy. Consequently, a phase transition from hexagonal to lamellar structures occurs, as the hexagonal configuration possesses a greater surface area. This was evidenced by observing the second phase transition at 120 °C, where the hexagonal structure converted to a lamellar structure, indicated by a shift in the q^* value and a characteristic peak ratio of $q^*/q = 1:2:3$. The third phase transition was detected at 150 °C, attributed to the transesterification reaction, leading to another structural rearrangement. Interestingly, the short-range order of cylinder structure reverted to a long-range order of HPC structure with lower q^* values, resulting in $q^* = 0.144$ nm^{-1} and a d-spacing of 43.6 nm, driven by thermal expansion. The B2P8/EC blend with an 80/20 ratio demonstrated a d-spacing of 38.0 nm at 25 °C, as depicted in Figure 7d. During thermal treatment, upon reaching 120 °C, the blend experienced its initial phase transition from a micelle-like structure to a long-range order of HPC structure, as depicted in Figure 9a by SAXS analyses (peak ratio of $1:\sqrt{3}:\sqrt{4}:\sqrt{9}$) and Figure 9d,g by TEM images. Unlike the previous blend, the structure of this blend remained stable, as observed in Figure 9b,e,h, likely due to the lower proportion of EC and the reduced impact of transesterification reactions. As the thermal treatment temperature escalated, the d-spacing continued to grow due to thermal expansion, eventually resulting in ordered sphere structures, as seen in Figure 9c,f,i again.

We conducted a thorough investigation of the self-assembled structures of B4P6/EC blends under various thermal treatments, as depicted in Figures 10a and 11a. Initially, B4P6/EC blends with a 60/40 ratio exhibited disordered miscible spheres with an d-spacing of 38.0 nm before any thermal treatment, as shown in Figure 10a. The first phase transition occurred at 60 °C, indicated by a peak ratio of $1:\sqrt{3}:\sqrt{4}$ with an HPC structure. As the thermal temperature escalated, the d-spacing expanded further. Subsequently, the blend system revealed a long-range order of sphere structure at 120 °C with $1:\sqrt{2}:\sqrt{3}:\sqrt{4}$, which was consistent with the TEM images presented in Figure 10b,c. However, TEM images at 150 °C showed the formation of a disordered phase, corresponding to the SAXS patterns outlined in Figure 10d,e, which also can be attributed to transesterification reactions. At 210 °C, both SAXS patterns and TEM images demonstrated a disordered spherical structure, as illustrated in Figure 10f,g.

In contrast, B4P6/EC blends with a 80/20 ratio initially revealed a short-range ordered hexagonal cylinder structure at room temperature, as shown in Figure 11a. With an escalating thermal treatment temperature, the q^* values shifted to lower q values as a result of thermal expansion. TEM images indicated that the blend maintained a hexagonal cylinder structure at 120 °C, as depicted in Figure 11b,c. At 150 °C, the occurrence of transesterification reactions led to a gradual transformation of the structure into an ordered sphere, with a d-spacing of 45.1 nm, as outlined in Figure 11d,e. By the time the thermal treatment temperature reached 210 °C, ordered spherical structures were consistently observed, as shown in Figure 11f,g.

This comprehensive analysis elucidates the structural transitions and thermal behavior of B4P6/EC blends, providing significant insights into their phase behavior and stability under varying thermal conditions. Following pyrolysis of B4P6/EC at a temperature of 470 °C for 1 day, the EC was

subsequently removed. The B4P6/EC blends with an 80/20 ratio revealed short-range ordered spheres with the peak ratio displaying $1:\sqrt{2}:\sqrt{3}:\sqrt{4}$, as shown in Figure 12a. The TEM image unveiled that the blend presented ordered spheres, while the SEM image displayed the spherical holes, as illustrated in Figure 12c,e. Conversely, Figure 12b shows that B2P8/EC with an 80/20 ratio presented disordered spheres, consistent with the TEM and SEM images depicted in Figure 12d,f.

CONCLUSIONS

To summarize, a functionalized vanillinazine monomer, VBAZ-2OH, was synthesized via an imine reaction. VBAZ-BZ-2OH was subsequently derived from VBAZ-2OH using ethanolamine and $(CH_2O)_n$ in DO as a solvent. The blends of VBAZ-BZ-2OH and EC demonstrated strong hydrogen bonding with the C−O−C groups of the PEO segment but weaker hydrogen bonding with the C=O groups of the PCL segment, thus preventing any competitive interactions. However, the addition of phenolic resin resulted in strong hydrogen bonding between the C−O−C groups of the PEO section and the C=O groups of the PCL block, leading to hydrogen-bonding competition, as shown by 1D and 2D FTIR spectra. This competition caused the observed microphase separation. Interestingly, at temperatures above 150 °C, an ordered phase transitioned into a disordered spherical phase in the B2P8/EC = 60/40 blends. This transition was due to a transesterification reaction, making EC miscible in VBAZ-BZ-2OH, as verified by TEM and SAXS analyses, to replace TGA-GC analyses.

ASSOCIATED CONTENT

ⓈⒾ Supporting Information

The Supporting Information is available free of charge at https://pubs.acs.org/doi/10.1021/acs.macromol.4c02072.

> Characterization methods, synthesis of PEO-*b*-PCL, summarized the molecular weights of PEO-*b*-PCL, summarized the melting and crystallization temperatures of various VBAZ-BZ-2OH/EC blends analyzed using DSC, the polymerization mechanism of the VBAZ-BZ-2OH monomer, ^{13}C NMR analysis of VBAZ-2OH, ^{13}C NMR analysis of VBAZ-BZ-2OH, summarized T_{d10} values and char yields of VBAZ-BZ-2OH, FTIR spectra and ^{1}H NMR spectra of PEO-*b*-PCL, DOSY spectrum of PEO$_{112}$-*b*-PCL$_{99}$, TGA thermograms of the VBAZ-BZ-2OH/EC blend with diverse compositions, summarized T_{d10} values and char yields of VBAZ-BZ-2OH, FTIR spectra for the C−O−C stretch of VBAZ-BZ-2OH/EC recorded at 25 °C, dynamic FTIR spectra for the VBAZ-BZ-2OH/EC = 60/40 blends, dynamic FTIR spectra for C−O−C groups of VBAZ-BZ-2OH/EC = 60/40 blends, DSC thermograms of B2P8 and B4P6, and FTIR spectra for the C−O−C stretch of B2P8/EC recorded at 25 °C (PDF)

AUTHOR INFORMATION

Corresponding Author

Shiao-Wei Kuo − *Department of Materials and Optoelectronic Science, Center for Functional Polymers and Supramolecular Materials, National Sun Yat-Sen University, Kaohsiung 804, Taiwan;* ⓞ orcid.org/0000-0002-4306-7171; Email: kuosw@faculty.nsysu.edu.tw

Authors

Yang-Chin Kao − *Department of Materials and Optoelectronic Science, Center for Functional Polymers and Supramolecular Materials, National Sun Yat-Sen University, Kaohsiung 804, Taiwan*

Yi-Hsuan Ku − *Department of Materials and Optoelectronic Science, Center for Functional Polymers and Supramolecular Materials, National Sun Yat-Sen University, Kaohsiung 804, Taiwan*

Mohamed Gamal Mohamed − *Department of Materials and Optoelectronic Science, Center for Functional Polymers and Supramolecular Materials, National Sun Yat-Sen University, Kaohsiung 804, Taiwan;* ⓞ orcid.org/0000-0003-0301-8372

Wei-Hung Su − *Department of Materials and Optoelectronic Science, Center for Functional Polymers and Supramolecular Materials, National Sun Yat-Sen University, Kaohsiung 804, Taiwan*

Complete contact information is available at:
https://pubs.acs.org/10.1021/acs.macromol.4c02072

Notes

The authors declare no competing financial interest.

ACKNOWLEDGMENTS

REFERENCES

(1) Eghbali, H.; Sadeghi, M.; Noroozi, M.; Movahedifar, F. Vanillin crosslinked 3D porous chitosan hydrogel for biomedicine applications: Preparation and characterization. *J. Mech. Behav. Biomed. Mater.* **2023**, *145*, No. 106044.

(2) da Silva, R. L.; Bernardinelli, O. D.; Frachini, E. C.; Ulrich, H.; Sabadini, E.; Petri, D. F. Vanillin crosslinked chitosan films: The states of water and the effect of carriers on curcumin uptake. *Carbohydr. Polym.* **2022**, *292*, No. 119725.

(3) Ma, J.; Li, G.; Hua, X.; Liu, N.; Liu, Z.; Zhang, F.; Yu, L.; Chen, X.; Shang, L.; Ao, Y. Biodegradable epoxy resin from vanillin with excellent flame-retardant and outstanding mechanical properties. *Polym. Degrad. Stab.* **2022**, *201*, No. 109989.

(4) Zhi, M.; Yang, X.; Fan, R.; Yue, S.; Zheng, L.; Liu, Q.; He, Y. Sustainable vanillin-based epoxy resin with excellent flame retardancy and mechanical properties. *ACS Appl. Polym. Mater.* **2023**, *5*, 1312−1324.

(5) Zhao, D.; Liang, X.; Wang, J.; Du, J.; Zhu, Y. Vanillin-based degradable polyurethane thermosets demonstrating high bio-content and mechanical properties. *ACS Appl. Polym. Mater.* **2023**, *5*, 4536−4545.

(6) Samy, M. M.; Mohamed, M. G.; Kuo, S. W. Directly Synthesized Nitrogen-and-Oxygen-Doped Microporous Carbons Derived from a Bio-Derived Polybenzoxazine Exhibiting High-Performance Supercapacitance and CO$_2$ Uptake. *Eur. Polym. J.* **2020**, *138*, No. 109954.

(7) Mărtău, G. A.; Călinoiu, L. F.; Vodnar, D. C. Bio-vanillin: Towards a sustainable industrial production. *Trends Food Sci.* **2021**, *109*, 579−592.

(8) Kao, Y. C.; Chen, W. C.; EL-Mahdy, A. F.; Mohamed, M. G.; Ejaz, M.; Kuo, S. W. Thermal Stable and Flexible Bio-Based Polybenzoxazine with Epoxy-Functionalized Poly(dimethylsiloxane) Hybrids. *Macromol. Chem. Phys.* **2023**, *224*, 2300153.

(9) Liu, Y.; Yuan, L.; Liang, G.; Gu, A. Developing thermally resistant and strong biobased resin from benzoxazine synthesized using green solvents. *Eur. Polym. J.* **2022**, *173*, No. 111320.

(10) Sha, X. L.; Fei, P.; Wang, X.; Gao, Y.; Zhu, Y.; Liu, Z.; Lv, R. Large free volume biobased benzoxazine resin: Synthesis and characterization, dielectric properties, thermal and mechanical properties. *Eur. Polym. J.* **2023**, *198*, No. 112420.

(11) Liu, Y.; Yuan, L.; Liang, G.; Gu, A. Preparation of Thermally Resistant and Mechanically Strong Biomass Benzoxazine Resins via Green Strategy. *ACS Sustain. Chem. Eng.* **2024**, *12*, 1247−1254.

(12) Lu, Y.; Liu, J.; Zhao, W.; Zhang, K. Bio-benzoxazine structural design strategy toward highly thermally stable and intrinsically flame-retardant thermosets. *Chem. Eng. J.* **2023**, *457*, No. 141232.

(13) Naiker, V. E.; Patil, D. A.; More, A. P.; Mhaske, S. T. Synthesis of high-performance bio-based benzoxazine for flame retardant application. *Polym. Adv. Technol.* **2022**, *33*, 1481−1495.

(14) Liu, J.; Sheng, W.; Yang, R.; Liu, Y.; Lu, Y.; Zhang, K. Synthesis of bio-diamine derived main-chain type benzoxazine resins with low surface free energy. *J. Appl. Polym. Sci.* **2023**, *140*, No. e53578.

(15) Ejaz, M.; Mohamed, M. G.; Chen, Y. T.; Zhang, K.; Kuo, S. W. Porous carbon materials augmented with heteroatoms derived from hyperbranched biobased benzoxazine resins for enhanced CO_2 adsorption and exceptional supercapacitor Performance. *J. Energy Storage* **2024**, *78*, No. 110166.

(16) Lu, Y.; Li, Q.; Zhang, Z.; Hu, X. Biobased dual-cure thiol-ene benzoxazine resins for high-performance polymer dielectrics. *Mater. Des.* **2022**, *224*, No. 111359.

(17) Klfout, H. A.; Asiri, A. M.; Alamry, K. A.; Hussein, M. A. Recent advances in bio-based polybenzoxazines as an interesting adhesive coating. *RSC Adv.* **2023**, *13*, 19817−19835.

(18) Appasamy, S.; Krishnasamy, B.; Ramachandran, S.; Muthukaruppan, A. Vanillin derived partially bio-based benzoxazine resins for hydrophobic coating and anticorrosion applications: Studies on syntheses and thermal behavior. *Polym.-Plast. Technol. Mater.* **2024**, *63*, 287−298.

(19) Marliana, M.; Hassan, A.; Yuziah, M. N.; Khalil, H. A.; Inuwa, I.; Syakir, M.; Haafiz, M. M. Flame retardancy, Thermal and mechanical properties of Kenaf fiber reinforced Unsaturated polyester/Phenolic composite. *Fibers Polym.* **2016**, *17*, 902−909.

(20) Chen, W. C.; Liu, Y. T.; Kuo, S. W. Highly Thermal Stable Phenolic Resin Based on Double-Decker-Shaped POSS Nanocomposites for Supercapacitors. *Polymers* **2020**, *12*, 2151.

(21) Adem, A. A.; Panjiar, H.; Daniel, B. S. S. The effect of nanocarbon inclusion on mechanical, tribological, and thermal properties of phenolic resin-based composites: An overview. *Eng. Rep.* **2024**, *6*, No. e12861.

(22) Chiou, C. W.; Lin, Y. C.; Wang, L.; Maeda, R.; Hayakawa, T.; Kuo, S. W. Hydrogen bond interactions mediate hierarchical self-assembly of POSS-containing block copolymers blended with phenolic resin. *Macromolecules* **2014**, *47*, 8709−8721.

(23) Mohamed, M. G.; Chang, W. C.; Kuo, S. W. Crown Ether- and Benzoxazine-Linked Porous Organic Polymers Displaying Enhanced Metal Ion and CO_2 Capture through Solid-State Chemical Transformation. *Macromolecules* **2022**, *55*, 7879−7892.

(24) Aly, K. I.; Mostafa Ebrahium, S.; Abdelhamid, H. N.; El-Bery, H. M.; Mohammed, A. A. K.; Huang, C. W.; Gamal Mohamed, M. Efficient synthesis of main chain thermosetting polybenzoxazine resin containing tert-butylcyclohexanone and diphenylmethane units for supercapacitor energy storage. *Eur. Polym. J.* **2024**, *221*, No. 113519.

(25) Ejaz, M.; Mohamed, M. G.; Kuo, S. W. Solid state chemical transformation provides a fully benzoxazine-linked porous organic polymer displaying enhanced CO_2 capture and supercapacitor performance. *Polym. Chem.* **2023**, *14*, 2494−2509.

(26) Lu, A.; Lin, H.; Yuan, M.; Shao, L.; Lu, X.; Xin, Z. Preparation of biphenyl-containing polybenzoxazines with low dielectric constants and high thermal stability. *Polymer* **2023**, *280*, No. 126018.

(27) Fan, X.; Liu, Z.; Huang, J.; Han, D.; Qiao, Z.; Liu, H.; Du, J.; Yan, H.; Ma, Y.; Zhang, C.; Wang, Z. Synthesis, curing mechanism, thermal stability, and surface properties of fluorinated polybenzox-

azines for coating applications. *Adv. Compos. Hybrid Mater.* **2022**, *5*, 322−334.

(28) Cai, W.; Wen, H.; Wang, Z.; Lu, H.; Liu, H.; Wang, Y.; Liu, W.; Wang, J.; Qiu, J. Design, synthesis, flame retardancy and dielectric properties of novel aromatic hyperbranched benzoxazine. *React. Funct. Polym.* **2022**, *170*, No. 105098.

(29) Wang, C. F.; Su, Y. C.; Kuo, S. W.; Huang, C. F.; Sheen, Y. C.; Chang, F. C. Low-Surface-Free-Energy Materials Based on Polybenzoxazines. *Angew. Chem., Int. Ed.* **2006**, *45*, 2248−2251.

(30) Mohamed, M. G.; Su, B. X.; Kuo, S. W. Robust Nitrogen-Doped Microporous Carbon via Crown Ether-Functionalized Benzoxazine-Linked Porous Organic Polymers for Enhanced CO_2 Adsorption and Supercapacitor Applications. *ACS Appl. Mater. Interfaces* **2024**, *16*, 40858−40872.

(31) Thubsuang, U.; Manmuanpom, N.; Chokaksornsan, N.; Sommut, C.; Singhawat, K.; Payaka, A.; Wongkasemjit, S.; Chaisuwan, T. Efficient CO_2 adsorption on porous carbon with nitrogen functionalities based on polybenzoxazine: high-pressure adsorption characteristics. *Appl. Surf. Sci.* **2023**, *607*, No. 155120.

(32) Mohamed, M. G.; Chen, T. C.; Kuo, S. W. Solid-State Chemical Transformations to Enhance Gas Capture in Benzoxazine-Linked Conjugated Microporous Polymers. *Macromolecules* **2021**, *54*, 5866−5877.

(33) Wang, W.; Liu, H.; Pei, L.; Liu, H.; Wang, M.; Li, S.; Wang, Z. Modified polybenzoxazine and carbon fiber surface with improved mechanical properties by introducing hydrogen bonds. *Eur. Polym. J.* **2023**, *182*, No. 111717.

(34) Li, Y. Y.; Li, Y. L.; Liu, L. N.; Xu, Z. W.; Xie, G.; Wang, Y.; Zhao, F. G.; Gao, T.; Li, W. S. Microporous N-and O-Codoped Carbon Materials Derived from Benzoxazine for Supercapacitor Application. *Inorganics* **2023**, *11*, 269.

(35) Fan, Z.; Li, B.; Ren, D.; Xu, M. Recent Progress of Low Dielectric and High-Performance Polybenzoxazine-Based Composites. *Polymers* **2023**, *15*, 3933.

(36) Gou, H.; Bao, Y.; Huang, J.; Fei, X.; Li, X.; Wei, W. Development of molding compounds based on epoxy resin/aromatic amine/benzoxazine for high-temperature electronic packaging applications. *Macromol. Mater. Eng.* **2022**, *307*, 2200351.

(37) Fan, X.; Li, S.; Wang, C.; Deng, Y.; Zhang, C.; Wang, Z. Research on fluoropyridine-based benzoxazine with high thermal stability and excellent flame retardancy for its application in coatings. *Eur. Polym. J.* **2023**, *187*, No. 111884.

(38) Lyu, Y.; Ishida, H. Natural-sourced benzoxazine resins, homopolymers, blends and composites: A review of their synthesis, manufacturing and applications. *Prog. Polym. Sci.* **2019**, *99*, No. 101168.

(39) Dyer, W. E.; Kumru, B. Polymers as Aerospace Structural Components: How to Reach Sustainability? *Macromol. Chem. Phys.* **2023**, *224*, 2300186.

(40) Lai, Y. C.; Lo, C. T. Hydrogen bonding induced microphase and macrophase separations in binary block copolymer blends. *Polymer* **2022**, *262*, No. 125501.

(41) Kuo, S. W. Construction Archimedean tiling patterns based on soft materials from block copolymers and covalent organic frameworks. *Giant* **2023**, *15*, No. 100170.

(42) Chen, W. C.; Kuo, S. W.; Jeng, U. S.; Chang, F. C. Self-assembly through competitive interactions of miscible diblock copolymer/homopolymer blends: Poly(vinylphenol-*b*-methyl methacrylate)/poly (vinylpyrrolidone) blend. *Macromolecules* **2008**, *41*, 1401−1410.

(43) Chou, T. C.; Kuo, S. W. Controllable Wet-Brush Blending of Linear Diblock Copolymers with Phenolic/DDSQ Hybrids toward Mesoporous Structure Phase Diagram. *Macromolecules* **2024**, *57*, 5958−5970.

(44) Kuo, S. W. Hydrogen bond-mediated self-assembly and supramolecular structures of diblock copolymer mixtures. *Polym. Int.* **2009**, *58*, 455−464.

(45) Balazs, A. C. Modeling self-assembly and phase behavior in complex mixtures. *Annu. Rev. Phys. Chem.* **2007**, *58*, 211−233.

(46) Chen, W. C.; Liu, Y. T.; Kuo, S. W. Mesoporous Organic/Inorganic Hybrid Materials with Frank-Kasper Phases Templated by an Unusual Linear Symmetry Diblock Copolymer. *Macromol. Rapid Commun.* **2021**, *42*, 2100302.

(47) Zhang, B.; Xie, S.; Lodge, T. P.; Bates, F. S. Phase behavior of diblock copolymer−homopolymer ternary blends with a compositionally asymmetric diblock copolymer. *Macromolecules* **2021**, *54*, 460−472.

(48) Huang, Y. C.; Chen, W. C.; Kuo, S. W. Mesoporous phenolic/POSS hybrids induced by microphase separation arising from competitive hydrogen bonding interactions. *Macromolecules* **2022**, *55*, 8918−8930.

(49) Mishra, A. K.; Lee, J.; Kang, S.; Kim, E.; Choi, C.; Kim, J. K. Gallol-based block copolymer with a high flory−huggins interaction parameter for next-generation lithography. *Macromolecules* **2022**, *55*, 10797−10803.

(50) Zenati, A.; Pokhrel, A. Properties and molecular self-assembly of liquid crystalline hard−hard diblock and hard−soft−hard triblock copolymers influenced by Flory−Huggins interaction parameter and volume fraction of distinct segments. *J. Polym. Sci.* **2023**, *61*, 1596−1611.

(51) EL-Mahdy, A. F.; Yu, T. C.; Mohamed, M. G.; Kuo, S. W. Secondary structures of polypeptide-based diblock copolymers influence the microphase separation of templates for the fabrication of microporous carbons. *Macromolecules* **2021**, *54*, 1030−1042.

(52) Li, J.; Ho, Y.; Ahmed, M. M. M.; Liang, H.; Kuo, S. Mesoporous carbons templated by PEO-PCL block copolymers as electrode materials for supercapacitors. *Chem.—Eur. J.* **2019**, *25*, 10456−10463.

(53) Li, J. G.; Lee, P. Y.; Ahmed, M. M.; Mohamed, M. G.; Kuo, S. W. Varying the hydrogen bonding strength in phenolic/PEO-*b*-PLA blends provides mesoporous carbons having large accessible pores suitable for energy storage. *Macromol. Chem. Phys.* **2020**, *221*, 2000040.

(54) Chu, W. C.; Li, J. G.; Kuo, S. W. From flexible to mesoporous polybenzoxazine resins templated by poly (ethylene oxide-*b*-ε-caprolactone) copolymer through reaction induced microphase separation mechanism. *RSC Adv.* **2013**, *3*, 6485−6498.

(55) Chou, T.; Chen, W.; Mohamed, M. G.; Huang, Y.; Kuo, S. Organic-Inorganic Phenolic/POSS Hybrids Provide Highly Ordered Mesoporous Structures Templated by High Thermal Stability of PS-b-P4VP Diblock Copolymer. *Chem.—Eur. J.* **2023**, *29*, No. e202300538.

(56) Li, J. G.; Chu, W. C.; Jeng, U. S.; Kuo, S. W. In Situ Monitoring of the Reaction-Induced Self-Assembly of Phenolic Resin Templated by Diblock Copolymers. *Macromol. Chem. Phys.* **2013**, *214*, 2115−2123.

(57) Banik, M.; Oded, M.; Shenhar, R. Coupling the chemistry and topography of block copolymer films patterned by soft lithography for nanoparticle organization. *Soft Matter* **2022**, *18*, 5302−5311.

(58) Liu, S.; Yang, Y.; Zhang, L.; Xu, J.; Zhu, J. Recent progress in responsive photonic crystals of block copolymers. *J. Mater. Chem. C* **2020**, *8*, 16633−16647.

(59) Huang, J.; Hall, A.; Jayapurna, I.; Algharbi, S.; Ginzburg, V.; Xu, T. Nanocomposites based on coil-comb diblock copolymers. *Macromolecules* **2021**, *54*, 1006−1016.

(60) Kuo, S. W. Hydrogen bonding mediated self-assembled structures from block copolymer mixtures to mesoporous materials. *Polym. Int.* **2022**, *71*, 393−410.

(61) Mohamed, M. G.; Atayde, E. C., Jr; Matsagar, B. M.; Na, J.; Yamauchi, Y.; Wu, K. C. W.; Kuo, S. W. Construction Hierarchically Mesoporous/Microporous Materials Based on Block Copolymer and Covalent Organic Framework. *J. Taiwan Inst. Chem. Eng.* **2020**, *112*, 180−192.

(62) Cheng, Y.; Mao, Q.; Zhou, C.; Huang, X.; Liu, J.; Deng, J.; Sun, Z.; Jeong, S.; Cho, Y.; Zhang, Y.; Huang, B.; Wu, F.; Yang, C.; Chen, L. Regulating the Sequence Structure of Conjugated Block Copolymers Enables Large-Area Single-Component Organic Solar Cells with High Efficiency and Stability. *Angew. Chem.* **2023**, *135*, No. e202308267.

(63) Koo, W. T.; Woo, S.; Shin, E.; Lee, J.; Lee, H.; Ku, K. H.; Kim, S. J.; Kim, I. D. Nanoscopic Catalyst-loaded Porous Metal Oxide Hollow Frameworks using Porous Block Copolymer Templates for High Performance Formaldehyde Sensors. *Sens. Actuators B: Chem.* **2024**, *418*, No. 136282.

(64) Wang, L.; Zhou, J.; Zhang, H.; Zou, H.; Chen, Y.; Liang, M.; Heng, Z. Nanostructure transformation in epoxy/block copolymer composites with good mechanical properties. *React. Funct. Polym.* **2022**, *176*, No. 105299.

(65) Heng, Z.; Wang, L.; Chen, F.; Zhou, J.; Zhang, H.; Zhang, X.; Sun, T.; Ling, Y.; Xia, S.; Liang, M.; Chen, Y.; Zou, H. In-situ constructing ultra-high-aspect-ratio core-shell nanostructures to achieve high-performance epoxy thermosets and their carbon fiber reinforced epoxy composites. *Chem. Eng. J.* **2022**, *448*, No. 137707.

(66) Li, L.; Peng, W.; Liu, L.; Zheng, S. Toughening of epoxy by nanostructures with ABA triblock copolymers: An influence of organosilicon modification of block copolymer. *Polym. Eng. Sci.* **2022**, *62*, 392−404.

(67) Dorfman, K. D. Frank−Kasper phases in block polymers. *Macromolecules* **2021**, *54*, 10251−10270.

(68) Adjaoud, A.; Marcolini, B.; Dieden, R.; Puchot, L.; Verge, P. Deciphering the Self-Catalytic Mechanisms of Polymerization and Transesterification in Polybenzoxazine Vitrimers. *J. Am. Chem. Soc.* **2024**, *146*, 13367−13376.

(69) Salvi, B. L. Transesterification methods. *Prod. Biodiesel Non-Edible Sources* **2022**, 117−151.

(70) Wang, B.; Wang, B.; Shukla, S. K.; Wang, R. Enabling catalysts for biodiesel production via transesterification. *Catalysts* **2023**, *13*, 740.

(71) Pandit, C.; Banerjee, S.; Pandit, S.; Lahiri, D.; Kumar, V.; Chaubey, K. K.; Al-Balushi, R.; Al-Bahry, S.; Joshi, S. J. Recent advances and challenges in the utilization of nanomaterials in transesterification for biodiesel production. *Heliyon* **2023**, *9*, No. e15475.

(72) Dong, B.; Xu, G.; Yang, R.; Guo, X.; Wang, Q. Preparation of Block Copolymers by a Sequential Transesterification Strategy: A Feasible Route for Upcycling End-of-Life Polyester Plastics to Elastomers. *Macromolecules* **2023**, *56*, 10143−10152.

(73) Sahani, S.; Jaiswal, S.; Mishra, S.; Sharma, Y. C.; Han, S. S. Recent advances in bio-glycerol valorization to glycerol carbonate by heterogenous base-catalyzed transesterification. *Mol. Catal* **2023**, *550*, No. 113508.

(74) Yaakob, M. N. A.; Salim, N.; Mustapha, S. N. H.; Misnon, I. I.; Ab Rahim, M. H.; Roslan, R. Exploring sustainable alternatives: Utilizing natural precursor for eco-friendly polybenzoxazine. *Polymer* **2024**, *302*, No. 127034.

(75) Lin, H. C.; Kuo, S. W.; Huang, C. F.; Chang, F. C. Thermal and Surface Properties of Phenolic Nanocomposites Containing Octaphenol Polyhedral Oligomeric Silsesquioxane. *Macromol. Rapid Commun.* **2006**, *27*, 537−541.

(76) Kuo, S. W.; Lin, H. C.; Huang, W. J.; Huang, C. F.; Chang, F. C. Hydrogen Bonding Interactions and Miscibility between Phenolic Resin and Octa(Acetoxystyryl) Polyhedral Oligomeric Silsesquioxane (AS-POSS) Nanocomposites. *J. Polym. Sci.; Part B: Polym. Phys.* **2006**, *44*, 673−686.

(77) Li, J. G.; Lin, Y. D.; Kuo, S. W. From microphase separation to self-organized mesoporous phenolic resin through competitive hydrogen bonding with double-crystalline diblock copolymers of poly(ethylene oxide-*b*-ε-caprolactone). *Macromolecules* **2011**, *44*, 9295−9309.

(78) Celik, S.; Ozkok, F.; Ozel, A. E.; Cakir, E.; Akyuz, S. Synthesis, FT-IR and NMR characterization, antibacterial and antioxidant activities, and DNA docking analysis of a new vanillin-derived imine compound. *J. Mol. Struct.* **2021**, *1236*, No. 130288.

(79) Rashid, M. A.; Mian, M. M.; Wei, Y.; Liu, W. A vanillin-derived hardener for recyclable, degradable and self-healable high-perform-

ance epoxy vitrimers based on transimination. *Mater. Today Commun.* **2023**, *35*, No. 106178.